ACS NANO

www.acsnano.org

High Thermal Conductivity of Submicrometer Aluminum Nitride Thin Films Sputter-Deposited at Low Temperature

Christopher Perez,* Aaron J. McLeod, Michelle E. Chen, Su-in Yi, Sam Vaziri, Ryan Hood, Scott T. Ueda, Xinyu Bao, Mehdi Asheghi, Woosung Park, A. Alec Talin, Suhas Kumar,* Eric Pop, Andrew C. Kummel, and Kenneth E. Goodson*

Cite This: https://doi.org/10.1021/acsnano.3c05485

Read Online

ACCESS | Metrics & More | Article Recommendations | SI Supporting Information

ABSTRACT: **Aluminum nitride (AlN) is one of the few electrically insulating materials with excellent thermal conductivity, but high-quality films typically require exceedingly hot deposition temperatures (>1000 °C). For thermal management applications in dense or high-power integrated circuits, it is important to deposit heat spreaders at low temperatures (<500 °C), without affecting the underlying electronics. Here we demonstrate 100 nm to 1.7 *μ*m thick AlN films achieved by low-temperature (<100 °C) sputtering, correlating their thermal properties with their grain size and interfacial quality, which we analyze by X-ray diffraction, transmission X-ray microscopy, as well as Raman and Auger spectroscopy. Controlling the deposition conditions through the partial pressure of reactive N_2, we achieve an ∼3× variation in thermal conductivity (∼36−104 W m^{-1} K^{-1}) of ∼600 nm films, with the upper range representing one of the highest values for such film thicknesses at room temperature, especially at deposition temperatures below 100 °C. Defect densities are also estimated from the thermal conductivity measurements, providing insight into the thermal engineering of AlN that can be optimized for application-specific heat spreading or thermal confinement.**

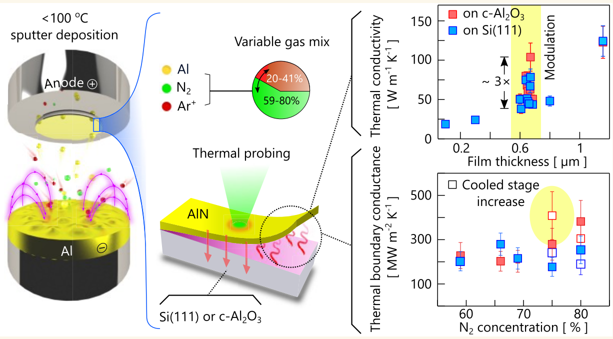

KEYWORDS: *thermal conductivity, aluminum nitride, back end of line, thermal transport, sputter deposition, low temperature, power electronics*

INTRODUCTION

Heat generation impedes the performance and longevity of nearly all modern electronic devices.[1−3] This is especially true in high-density integrated circuits[4] and power or radio-frequency (RF) electronics,[3,5] where elevated temperatures reduce transistor performance, increase leakage, and ultimately diminish device lifetimes.[6,7] A mere 5 °C increase in temperature above the optimum operating range can halve the lifetime of some devices.[7,8] Thermal management could be achieved by actively tuning heat flow and managing thermal transients, e.g. with the use of emerging thermal transistors and diodes.[9−11] Passive approaches involve simply using thin films to block or route heat away from hot spots in electronics. Such heat spreaders must have high thermal conductivity, but they must often be electrical insulators to prevent cross-talk between components—a set of properties that are common to only a few materials, such as aluminum nitride (AlN), boron nitride (BN), and diamond.

In particular, AlN has attracted much attention due to its large band gap (roughly 6.1 eV)[12,13] and bulk thermal conductivity (approximately 340 W m^{-1} K^{-1} at room temperature, or 85% the thermal conductivity of copper).[14−17] Indeed, bulk-like thermal conductivities have been demonstrated for AlN films on the order of hundreds,[16] tens,[18] and a few micrometers[19−21] in thickness, but such films are typically deposited at over 1200 °C. High temperatures are incompatible with many requirements of fabricating integrated circuits, where low-temperature (e.g., <500 °C for < 2 h) deposition is required for back-end-of-line (BEOL) processes.[22−24] More-

Received: June 17, 2023
Accepted: August 31, 2023
Published: October 5, 2023

ACS Publications

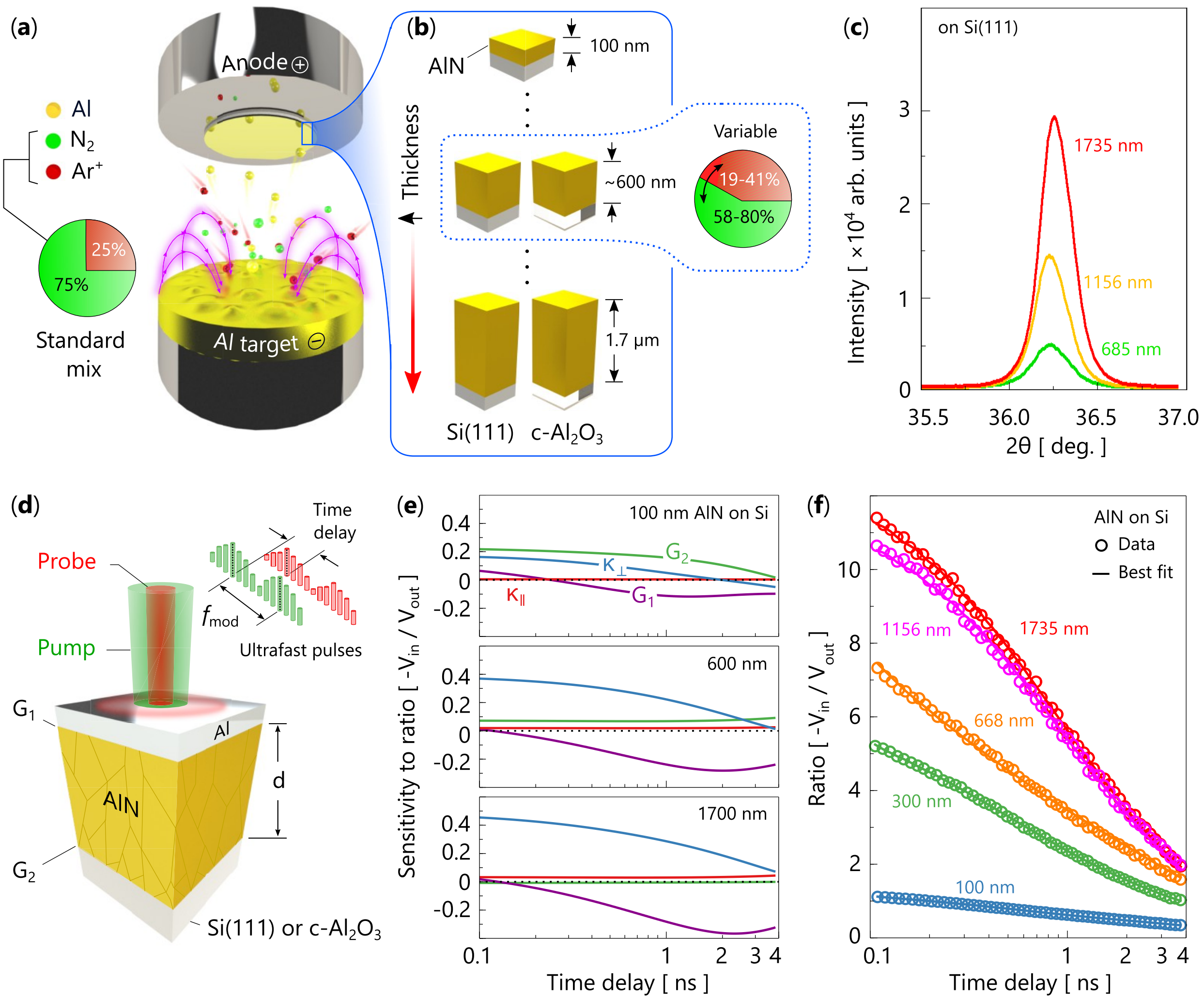

Figure 1. Experimental overview. (a) Illustration of our balanced DC magnetron sputtering deposition of AlN films using a standard sputter gas mix of 25% Ar and 75% N_2. (b) Schematic of the AlN film thickness variations explored in this work, along with their deposition on both Si(111) and c-Al_2O_3. The ~600 nm films are used to highlight the tuning of thermal conductivity by manipulating the sputtering gas composition. (c) Bragg−Brentano X-ray diffraction (XRD) spectra shown for the AlN films of various thicknesses deposited on Si(111), the results of which are used to estimate the grain size. (d) Simplified schematic of the TDTR measurement of the multilayer stack of materials used to determine thermal properties of the AlN films via detection of the sample response to periodic heating at a modulation frequency (f_{mod}). (e) Sensitivity of the TDTR ratio ($-V_{in}/V_{out}$) to the cross- and in-plane thermal conductivity ($\kappa_\perp/\kappa_\parallel$), Al/AlN thermal boundary conductance (G_1), and AlN/substrate thermal boundary conductance (G_2). (f) Characteristic model fits for the AlN films on Si ranging from $d \approx$ 100 to 1735 nm in thickness. Input properties for these calculations are provided in Section S5 of the Supporting Information.

over, integrated electronics would also benefit from thinner, microscale films of AlN, whose thermal conductivity has not been optimized and whose thermal limits are poorly understood. Devices fabricated with AlN heat spreaders, for example, can be complex and the literature remains unclear as to the dominant phonon scattering mechanisms in submicrometer versions of these materials.[25,26]

In this work, we demonstrate AlN films deposited by low-temperature (<100 °C) DC reactive balanced magnetron sputtering, with thicknesses ranging from 100 nm to 1.7 μm. The thermal conductivity of the films is determined by time-domain thermoreflectance (TDTR) and is correlated with microstructural properties, such as grain size and morphology, as determined by X-ray diffraction (XRD) and transmission electron microscopy (TEM), respectively. For films around 600 nm in thickness, we find the cross-plane thermal conductivity can be tuned by a factor of 3 by controlling the sputtering gas composition during deposition, with the upper end (~104 W m^{-1} K^{-1}) representing one of the highest values for this thickness at room temperature and at such low, BEOL-compatible deposition temperatures. Comparing these results with models based on the Boltzmann transport equation (BTE) for phonons shows that defect densities are being modulated by over an order of magnitude to produce the variation in thermal conductivity in our AlN films.

RESULTS AND DISCUSSION

AlN films were deposited using balanced DC sputtering,[27,28] as depicted in Figure 1a. Two series of AlN films were deposited (Figure 1b); the first used a standard gas composition of 25% Ar and 75% N_2 with film thicknesses of 685, 1156, and 1735 nm on both Si(111) and c-Al_2O_3 substrates shown in Figure 1a. The data for these films are summarized in Table 1, and deposition details can be found in Section S1 in the Supporting Information.

Table 1. Thickness, thermal conductivity, AlN (002) diffraction eak width, and estimated grain size (GS) for films of varied thickness deposited using a 75% N_2 and 25% Ar mixture on a non-chilled sample stage

substrate	d (nm)	κ (W m^{-1} K^{-1})	(002) fwhm (deg)	GS (nm)
Si(111)	100	18.7 ± 4.6	0.998	9.0
Si(111)	300	25.5 ± 4.7	0.660	13.2
Si(111)	647	51.1 ± 5.0	0.260	33.6
Si(111)	800	48.1 ± 6.4	0.620	14.0
Si(111)	1156	124.3 ± 19.4	0.194	45.2
Si(111)	1735	125.7 ± 21.4	0.186	47.0
c-Al_2O_3	647	68.1 ± 8.6	0.207	42.2
c-Al_2O_3	1156	122.8 ± 20.4	0.195	44.8
c-Al_2O_3	1735	118.9 ± 18.4	0.152	57.5

The second series of films approximately 600 nm in thickness were grown to demonstrate the tunability of the room-temperature (RT) thermal conductivity (κ) by manipulating the sputtering gas composition. Deposition details for these films can be found in Table 2 using both Si(111) and c-sapphire substrates with gas compositions varying from 19% to 41% Ar and from 58% to 80% N_2, shown in Figure 1b. Two of the samples in this series were deposited using a stage cooled to 10 °C. Additional films for this series were deposited using Kr in place of Ar, with details presented Section S2 in the Supporting Information. The films were characterized by Bragg−Brentano X-ray diffraction (XRD), an example of which is shown for the set of films with varied thickness in Figure 1c (Section S3 in the Supporting Information). In addition, high-resolution transmission electron microscopy (HR-TEM) was performed on the most thermally dissimilar samples. Time domain thermoreflectance (TDTR), as seen in Figure 1d−f, was performed on all films to measure their cross-plane thermal conductivity. Raman spectroscopy was also carried out to assess the film quality by means of characteristic E_2^2 modes and narrow full-width at half-maximum (fwhm) values,[29] shown in Section S4 of the Supporting Information.

A schematic of the AlN film specimens measured in this work is displayed in Figure 1d, consisting of an aluminum (Al) optothermal transducer, the AlN film, and a Si(111) or c-Al_2O_3 substrate. Thermal properties were determined by TDTR (Section S5 in the Supporting Information), an optical pump−probe technique described extensively in our prior works.[30−32] In TDTR, an ultrafast laser is used to both induce (pump) and monitor (probe) modulated heating on the surface of the sample as a function of pump−probe time delay. The thermal conductivity and thermal boundary conductances are then determined by fitting the intensity of the ratio ($-V_{in}/V_{out}$) signal of the reflected probe laser to a three-dimensional (3D) heat diffusion model for a multilayer stack of materials. Given the measurement conditions provided in Materials and Methods, the measurement is primarily sensitive to cross-plane thermal conductivity ($\kappa = \kappa_\perp$), as shown by the sensitivity calculations displayed in Figure 1e, which displays the sensitivity of the TDTR signal to the relevant properties for 100−1700 nm thick AlN films on a Si(111) substrate (see Section S6 in the Supporting Information). This is attributed to the disparity between the root-mean-square (RMS) average laser spot radius (w_{RMS}) and the in-plane thermal penetration depth that induces one-dimensional (1D) heat transfer.[33]

The high thermal conductivity and submicrometer thicknesses of these AlN films complicate the extraction of thermal properties and thus warrant an optimization approach. As the thermal penetration depth into the sample becomes comparable to the film thicknesses, the thermal boundary conductances on either side of the film increasingly influence the total thermal resistance of the measured system. As seen in Figure 1e, both the Al/AlN and AlN/Si interfaces (G_1 and G_2, respectively) contribute prominently to the thermal response for a 100 nm AlN film, while the AlN/Si interface becomes insensitive with a 1700 nm AlN film, i.e. it is thermally thick. For the ~600 nm films, however, the contribution of the AlN/Si interface is diminished but still significant. As shown in Section S7 of the Supporting Information, a global optimization sweeping the typical range of semiconductor−-dielectric interfaces[34] was performed to extract the thermal boundary conductances and intrinsic conductivities that provided the best fit to our thermal model with the lowest uncertainty, examples of which are shown in Figure 1f. Films on c-Al_2O_3 were analyzed in a similar manner but with slightly greater uncertainties in the thermal interfaces due to the

Table 2. Deposition conditions, film thicknesses, thermal conductivities, AlN (002) diffraction peak full-width at half-maximum (FWHM) Values, and estimated grain size (GS) for the measured films deposited using various sputtering gas compositions

substrate	cooled?	N_2 (%)	Ar (%)	d (nm)	κ (W m^{-1} K^{-1})	(002) FWHM (deg)	GS (nm)
c-Al_2O_3		59	41	645	48.3 ± 5.0	0.262	33.3
c-Al_2O_3		66	34	607	36.1 ± 3.8	0.303	28.8
c-Al_2O_3		69	31	600	50.8 ± 6.2	0.185	47.2
c-Al_2O_3		75	25	685	50.6 ± 3.3	0.168	52.0
c-Al_2O_3	Y	75	25	670	103.9 ± 17.9	0.126	69.3
c-Al_2O_3		80	20	639	74.9 ± 6.4	0.215	40.6
c-Al_2O_3	Y	80	20	668	62.9 ± 6.9	0.222	39.4
Si(111)		59	41	645	43.2 ± 4.3	0.242	36.1
Si(111)		66	34	607	38.1 ± 3.2	0.198	44.1
Si(111)		69	31	600	50.2 ± 5.4	0.205	42.6
Si(111)		75	25	685	43.7 ± 4.2	0.222	39.3
Si(111)	Y	75	25	670	78.5 ± 10.3	0.168	52.0
Si(111)		80	20	639	79.8 ± 5.5	0.177	49.3
Si(111)	Y	80	20	668	66.9 ± 8.4	0.185	47.2

increased contribution of the substrate to the probed thermal resistance.[35]

The measured cross-plane thermal conductivities of our AlN films are displayed in Figure 2a and compared to values from the literature[18−20,29,34,36−41] as a function of deposition temperature. Red, green, and blue symbols mark films greater than 2 μm, 1−2 μm, and less than 1 μm in thickness, respectively. The results of this study represent some of the highest reported thermal conductivities for submicrometer thin AlN films when considering the low deposition temperature of under 100 °C. The substrates were not actively heated during deposition, though a thermocouple placed under the substrate holder allowed for temperature monitoring. With initial stage cooling to 10 °C, temperature saturation due to plasma exposure during deposition occurred at 70 °C, lower than the 90−100 °C observed for samples deposited without stage cooling. In contrast, most chemical and physical deposition methods rely on heating substrates to several hundred degrees Celsius to effectively crystallize deposited material, producing films with greater thermal conductivity.

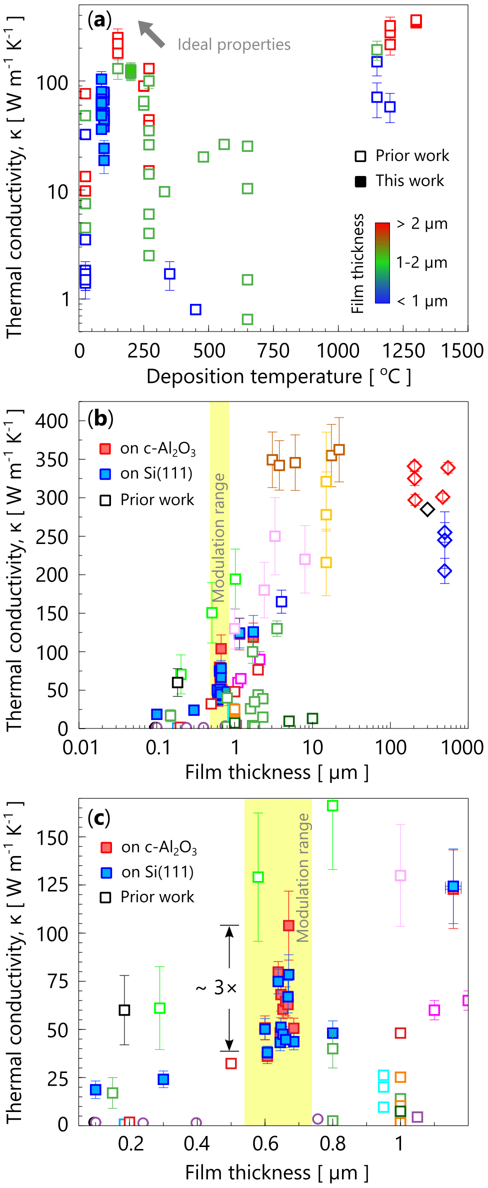

Figure 2. Room-temperature cross-plane thermal conductivity of our AlN films (filled square symbols) as functions of (a) deposition temperature and (b) thickness, compared to results from the literature.[18,19,29,34,36−42] In (b), diamond symbols are single-crystal samples: Slack[43] (black), Rounds[44] (red), and Xu[16] (blue). Square symbols are for polycrystalline films: Kuo[19] (orange), Jacquot[45] (light blue), Zhao[36] (purple), Choi[37] (red), Pan[39] (cyan), Aissa[40] (pink), Duquenne[38] (green), Alvarez-Escalante (light green),[42] Bian[41] (dark green), Yalon[29] (black), Cheng[18] (yellow), Koh[20] (brown), and Bellerk[46] (magenta). Round symbols correspond to amorphous thin films: Zhao[36] (purple) and Gaskins[34] (black). We note that the reported thermal conductivities are either isotropic or cross-plane to make for a fair comparison to our results and that nearly all films have deposition temperatures much greater than ours. The yellow shaded region marks the range of thicknesses wherein we demonstrate the modulation of thermal conductivity via a structure−processing−property relationship, magnified in (c) to show a ∼3× change.

The thermal conductivities of our AlN films sputtered at BEOL-compatible temperatures are compared with results from other studies as a function of film thickness in Figure 2b; these results are represented by filled symbols that are either red or blue, for films on c-Al_2O_3 and Si(111), respectively. In the submicrometer regime, the high thermal conductivity of our films indicates decreased defect density and reduced boundary scattering effects that typically plague nonepitaxial thin films, regardless of deposition technique. Indeed, minimizing defect densities and promoting the growth of larger grains is the primary focus of thin-film synthesis in electronic heat-spreading applications.[47,48] The yellow shaded region in Figure 2b shows the range of thermal conductivities achieved in this work by varying the sputtering deposition conditions. Figure 2c magnifies this region to show that the AlN thermal conductivity for the set of ∼600 nm films can range from ∼36 to ∼104 W m^{-1} K^{-1}: a nearly 3-fold change.

The modulation of thermal conductivity via a structure−processing−property relationship in these AlN films by tuning the sputtering gas composition was employed to understand the underlying mechanisms of improvement. Figure 3a plots the thermal conductivity with respect to the N_2 gas concentration of the ∼600 nm films on both c-Al_2O_3 and Si(111) in red and blue, respectively, with open symbols representing samples deposited using a cooled stage. We note that the balance gas for sputtering is Ar such that it comprises the full gas mixture, i.e., Ar(%) = 1 − N_2(%). Deposition on a noncooled stage with lower N_2 concentrations of 59−75% yielded lower thermal conductivity values ≤ 0 W m^{-1} K^{-1}. Conversely, an 80% N_2 deposition environment produced the most thermally conductive film among those that were not cooled. This is in contrast to work by Shinoda et al.,[49] who implemented a low N_2 concentration of 30% to produce films of high crystallinity, though with RF reactive magnetron sputtering and substrate temperatures exceeding 900 °C. In contrast, Kumada et al.[50] reported optimal N_2 concentrations of 40−50%, but with lower substrate temperatures of approximately 500 °C.

The general trend between higher N_2 concentrations and lower substrate temperatures, in the literature and in this work, highlights the complex interplay between process parameters: it is possible that at lower deposition temperatures, higher concentrations of N_2 are necessary to ensure complete nitridation of the deposited material. Further obscuring these relationships is the interplay of throw distance and ion mean free path, which itself is dependent upon a combination of pressure, applied power, and magnetic configuration of the

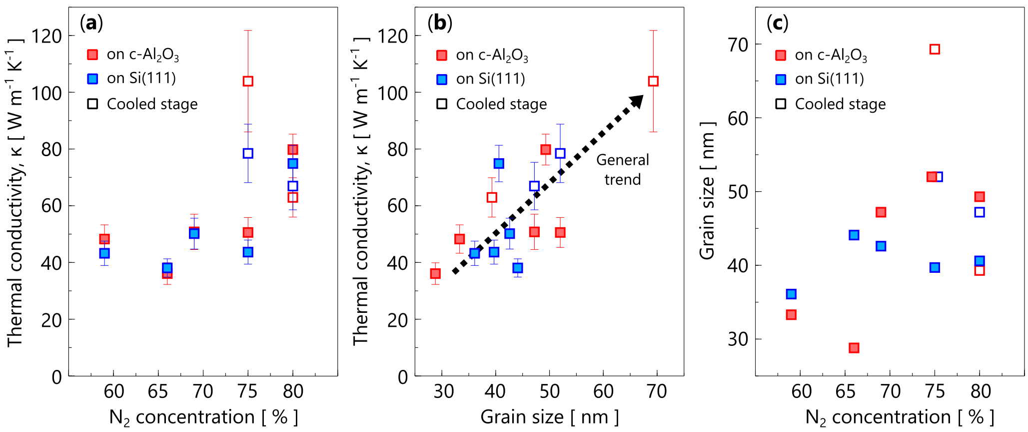

Figure 3. Correlations among thermal conductivity, grain size, and gas composition for ∼600 nm AlN films. (a) Thermal conductivity with respect to N_2 concentration and (b) grain size. The relationship between grain size and thermal conductivity is consistent with the importance of grain boundary scattering on thermal transport. Open squares represent films deposited on a cooled stage and exhibit the largest thermal conductivities. (c) Grain size with respect to the N_2 concentration. Note that the data at 75% N_2 concentration are slightly offset laterally for clarity.

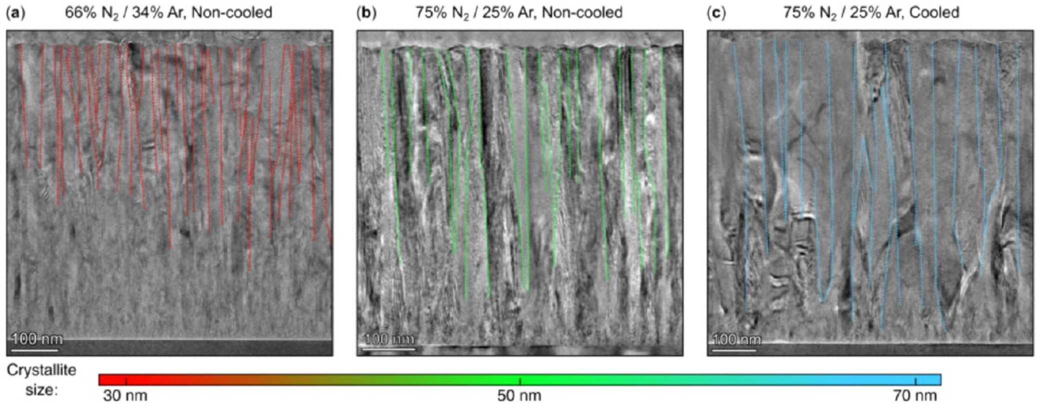

Figure 4. Transmission electron micrographs showing the full grain morphology for three sputtered films on c-Al_2O_3 using different conditions: (a) 66% N_2 and 34% Ar on a nonchilled stage, (b) 75% N_2 and 25% Ar without stage cooling, and (c) 75% N_2 and 25% Ar with the stage cooled to 10 °C throughout deposition. Grain boundaries are outlined to guide the eye.

sputtering equipment. Altering these parameters, directly or indirectly, affects the extent to which the reaction occurs in the plasma as well as the energetics of species bombarding the growth surface.[51] Careful tuning is necessary to ensure that the structure of the deposited material is tailored to enhance the properties of the material for the intended application.

Surprisingly, depositions with a cooled stage produced the most thermally conductive films in this work and some of the highest values reported in the field. Average grain sizes (GSs), are provided in Figure 3b, estimated using the fwhm of the AlN (002) diffraction peak and the Debye−Scherrer equation, revealing a positive correlation between grain size and thermal conductivity. Such a trend is consistent with decreased phonon scattering at grain boundaries, which is often the dominant scattering mechanism in dielectrics and semiconductors.[52] For clarity, these data are combined in Figure 3c to show the generally positive correlation among thermal conductivity, nitrogen content, and average grain size. It is well established that increasing the substrate temperature enhances surface migration and thus, crystalline quality. However, increased compressive stress at the AlN/substrate interface can occur during the postdeposition cooling process,[50] which can play a major role in determining overall crystallinity.[53] It is interesting to note that the stage-cooled films deposited with an 80% N_2 gas concentration become slightly less thermally conductive than their uncooled counterparts, suggesting an optimization among the aforementioned effects. Thermal measurements of AlN films deposited with Kr gas in place of Ar were also performed (see Section S2 in the Supporting Information) but demonstrated only moderate improvement with stage cooling.

TEM was performed on three films deposited on c-Al_2O_3 to gain insight into the microstructural features that influence transport. Figure 4 shows cross sections of two films deposited without stage cooling: (a) the most thermally insulating film deposited using 66% N_2 and (b) a film deposited using 75% N_2 with a larger thermal conductivity value. Grain boundaries are outlined to reveal a noticeable difference in their size and frequency, in agreement with both the estimated grain sizes and the thermal conductivity values (∼38 and ∼50 W m^{-1} K^{-1}, respectively). Figure 4c is shown to isolate the effect of the cooled stage, since the film was also deposited using 75% N_2. With grain sizes of roughly 70 nm, this film is also the most thermally conductive reported in this work (∼104 W m^{-1} K^{-1}) and clearly exhibits larger grains than either of the films presented.

Further inspection of the HR-TEM images suggests that the state of the film−substrate interface is a potential driver of transport, as shown in Figure 5. Analysis by a fast Fourier

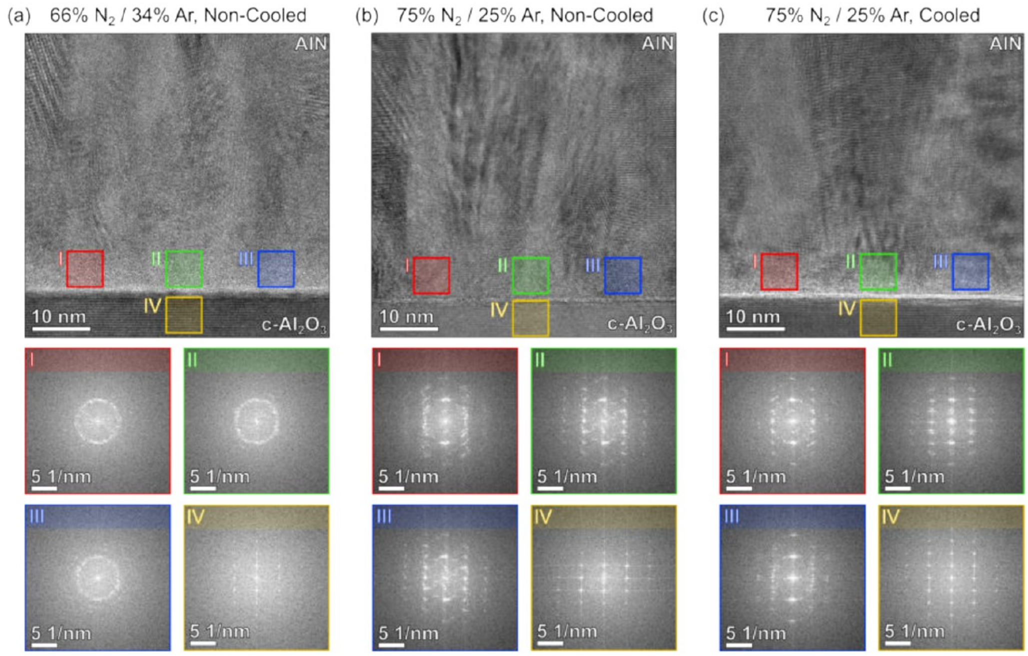

Figure 5. HR-TEM and FFT analysis of film crystallinity at the substrate interface of three key films deposited on c-Al_2O_3 using different conditions: (a) 66% N_2 and 34% Ar on a non-cooled stage, (b) 75% N_2 and 25% Ar without stage cooling, and (c) 75% N_2 and 25% Ar with the stage cooled to 10 °C throughout deposition.

transform (FFT) is provided for each film in three different near-interface regions (I−III) and for each underlying c-Al_2O_3 substrate (IV) for comparison. An amorphous layer develops at the AlN/c-Al_2O_3 interface for the film deposited with 66% N_2, further confirmed by the presence of rings rather than discrete diffraction spots in Figure 5a, I−III. This amorphous layer may be the result of an excess of energetic Ar ions bombarding the growth surface during initial deposition, resulting in amorphization at the initial stages of growth, as observed in existing literature reports.[19] This effect is reduced for both films deposited using 75% N_2, using the noncooled and cooled stages in Figure 5b,c, respectively. Both of these films exhibit stronger crystallinity above the interface and an "abrupt" character that is more prominent still for the film deposited with a cooled stage. It is likely that the substrate cooling in Figure 5c may have minimized adatom mobility during the initial growth, considering established qualitative models attributing such mobility to larger nucleation sites for crystal growth.[50] However, lower substrate temperatures can also provide a more favorable thermodynamic environment for the formation of nuclei, thereby leading to the formation of more uniformly sized and evenly distributed crystallites. Coupled with suspected reduced strain due to higher quality interfaces, both effects can lead to a more relaxed crystal lattice structure upon cooling, resulting in fewer defects and a more ordered crystal structure.[54−56] In practice, these effects are most easily observed in the larger and more uniformly sized crystallite columns in Figure 4c as compared with Figure 4b.

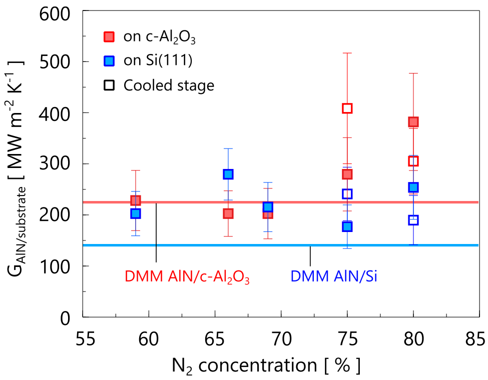

Figure 6. AlN/substrate thermal boundary conductances ($G_{\mathrm{AlN/substrate}}$) determined for our AlN films deposited on both Si(111) and c-Al_2O_3. We note the increasing trend of the AlN/ubstrate thermal boundary conductance upon stage cooling, suggesting the creation of a more well-matched interface, further reinforced with the TEM analysis in Figure 5. All data are from the present study.

Thermal boundary conductance measurements of the AlN/substrate interface reaffirm our microstructural results and lend validity to the most thermally conductive films reported in this work. As shown in Figure 6, the extracted AlN/substrate thermal boundary conductance values are compared with predictions from the diffuse mismatch model (DMM)[57,58] with a Born−von Karman (BVK) phonon dispersion approximation (see Section S8 in the Supporting Information). The DMM thermal boundary conductance (G_{DMM}) from material A to B is given by

$$G_{\mathrm{A}\to \mathrm{B}} = \frac{1}{4}\sum_{j}\int_{0}^{\infty} v_{\mathrm{A},j}\hbar\omega D_{\mathrm{A}}(\omega)\frac{\partial f_{\mathrm{BE}}^{0}(\omega, T)}{\partial T}\alpha_{\mathrm{A}\to \mathrm{B}}\, \mathrm{d}\omega \tag{1}$$

where j is the phonon branch, v is the phonon velocity in material A, $D_{\mathrm{A}}(\omega)$ is the phonon density of states in material A at phonon frequency ω, f_{BE}^{0} is the Bose−Einstein equilibrium function, and $\alpha_{A\to B}$ is the transmissivity from material A to B. Despite the DMM's inability to capture atomic-scale interface characteristics,[59] it is in broad agreement with our measured values for samples deposited with a noncooled stage, ranging from ~170 to ~280 MW m^{-2} K^{-1}. However, the general effect

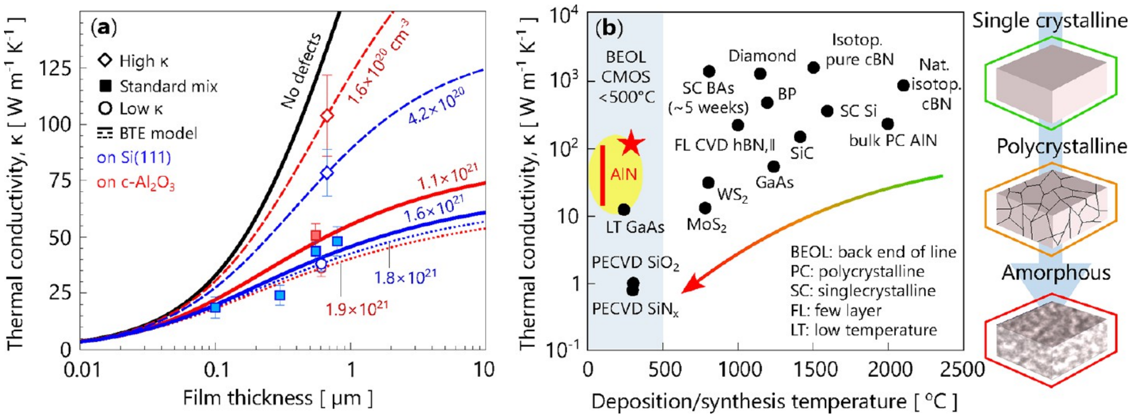

Figure 7. Thermal conductivity with respect to (a) the film thickness for samples in this study and (b) the deposition or synthesis temperature. In (a), the lines correspond to BTE predictions of eq 2 by fitting a defect density to the experimental data, revealing a modulation of roughly 1 order of magnitude. Here, high and low κ refer to the highest and lowest thermal conductivity films reported in this work. (b) Plot of thermal conductivity as a function of deposition temperature demonstrating the appeal for BEOL-compatible deposition of AlN films with high thermal conductivity relative to other materials commonly used in electronic devices.[16,43,65−74]

of a cooled stage is to increase the AlN/substrate thermal boundary conductance, as shown by the open symbols in Figure 6. This increase is more notable for AlN on c-Al$_2$O$_3$, which is also the substrate that produced our most thermally conductive film, attributed to more favorable lattice matching compared to Si(111). Indeed, stage cooling also increased the AlN/substrate thermal boundary conductance of films deposited with Kr gas in place of Ar, thus reinforcing this trend. Though large uncertainties prevent a more decisive conclusion due to suppressed sensitivities typical of embedded interfaces, the sharp increase of thermal boundary conductances is evident. This is important from a device perspective, where high-quality interfaces not only promote crystalline growth but can also dissipate more thermal energy to mitigate high operating temperatures and hot spots.[31] A summary of all conductance values is provided in Section S9 in the Supporting Information.

The underlying phonon scattering mechanisms in these AlN films were analyzed with an analytical model based on the Boltzmann transport equation (BTE). We employed a treatment of the BTE in a paradigm similar to past works[16,60−62]

$$\kappa = \frac{1}{3}Cv\lambda = \frac{1}{3}\sum_j \int_0^{\omega_{\max}} \hbar\omega D(\omega)\frac{\partial f^0_{\mathrm{BE}}(\omega, T)}{\partial T} v_j^2 \tau_j(\omega)\, \mathrm{d}\omega \tag{2}$$

where C is the volumetric heat capacity, λ is the phonon mean free path, $\omega_{\max}$ is the Debye cutoff frequency, and $\tau(\omega)$ is the phonon relaxation time. Umklapp, defect, and boundary scattering comprise the relaxation time and are summed in accordance with Matthiessen's rule (see Section S10 in the Supporting Information). Specifically, the point defect scattering rate can be expressed as[63]

$$\frac{1}{\tau_{\mathrm{D}}} = \frac{V}{4\pi v^3}\omega^4 \sum_i f_i \left(\frac{m - m_i}{m}\right)^2 \tag{3}$$

where f_i is the fractional concentration of the ith impurity atom and m and m_i are the masses of the orinal and ith impurity atoms, respectively. We make an important simplification in light of previous studies[16,64] that suggest Al vacancies play a dominant role due to the large atomic mass difference between Al and common impurities (e.g., Si, O, C, and N atoms). As such, the Al defect density is used as a fitting parameter in conjunction with our experimental data.

The foregoing BTE model sheds light on the degree of defect modulation occurring in our AlN films, as shown in Figure 7a. Here, a solid black line is provided to indicate the model behavior in the limit of no defects, and a fit of the model to the thickness-dependent experimental data using the standard 75% N$_2$ composition is also shown for comparison. We note that the defect-free thermal conductivity of ~600 nm thick AlN is ~150 W m^{-1} K^{-1}, suggesting that we reached up to 66% of this limit in the present work, even with films deposited at sub-100 °C temperature. In addition, changing the sputter gas composition alters the defect densities in the present films by over an order of magnitude, from 1.6×10^{20} to 1.9×10^{21} cm^{-3}. Such values are in agreement with similar predictions for AlN films, although even the purest films still possess a defect density an order of magnitude greater than that of the bulk.[16] Clearly, Al vacancies play a role in transport that is further elucidated by complementary electrical measurements detailed in Section S11 in the Supporting Information. Our electrical breakdown tests point to a larger relative dielectric constant in the 11.5−11.9 range for our standard 75% N$_2$ composition (the relative dielectric constant[34] of bulk AlN is ~9.2). Following measurements with Auger electron spectroscopy (Section S4 in the Supporting Information), the AlN films exhibit Al-rich compositions, which are suspected to increase the polarization character of AlN and the accompanying dielectric constant. This is in contrast to Al vacancies, which tend to decrease the dielectric constant. Although more rigorous characterization is needed to deduce the exact impurities present, these results nonetheless provide an intricate set of thermal interface and intrinsic thermal conductivity properties that can be tuned to a great degree.

Finally, Figure 7b provides a landscape of other materials used in electronic devices with respect to deposition temperature.[16,43,65−74] There is broadly a positive correlation between the thermal conductivity and deposition temperature in all the materials shown that is emphasized by the multicolored arrow. In this context, materials exhibiting both high thermal conductivity and electrical resistivity deposited at

https://doi.org/10.1021/acsnano.3c05485

low temperatures are desirable. Our results substantiate the modulation of thermal conductivity via a structure−processing−property relationship while maintaining <500 °C BEOL temperatures using WBG materials and are thus attractive candidates for integration in electronic applications requiring high operating frequencies and the handling of high power density.[3,5]

CONCLUSION

We studied sputter-deposited AlN films between 100 nm and 1.7 μm thicknesses, revealing the highest thermal conductivity reported to date in ∼600 nm films with low deposition temperature (<100 °C). At the ∼600 nm thickness, we also observed an ∼3× change in thermal conductivity by controlling the sputtering gas composition during deposition. We elucidated these effects via direct characterization by XRD, TEM, and HR-TEM, which complemented thermal conductivity measurements by TDTR. Analytical models of thermal conductivity based on the Boltzmann transport equation reveal estimated defect densities varying over an order of magnitude, between 1.6×10^{20} and 1.9×10^{21} cm^{-3}. The highest thermal conductivity values are found for depositions onto a cooled stage, which improved the film morphology. Across the entire sample set, correlations between thermal conductivity and microstructure confirm the importance of grain size and the quality and uniformity of the interfacial crystallinity, which are further reinforced by measurements of the thermal boundary conductance. Overall, these results show the potential of AlN as a heat-spreading material with low-temperature BEOL-compatible deposition parameters that can offer application-specific strategic heat spreading or thermal confinement.

MATERIALS AND METHODS

AlN Film Deposition. Sputtered AlN films were deposited using 100 W DC power on a 2 in. Al target after a standard target cleaning and conditioning procedure. All substrates were degreased with a series of solvent rinses. Si substrates were cleaned using a cyclic 2% HF etch, and c-Al_2O_3 substrates were cleaned by soaking in a 3:1 sulfuric acid and phosphoric acid mixture. More detailed descriptions of these procedures can be found in Section S1 in the Supporting Information.

Diffraction, Ellipsometry, and Transmission Electron Microscopy. Following deposition of the AlN films, all samples were analyzed by Bragg−Brentano X-ray diffraction (XRD) to assess their crystallinity. Grain sizes were estimated by the Debye−Scherrer formula based on AlN (002) diffraction peak full-width at half-maximum (fwhm) fits determined using Rigaku GlobalFit software, as described in Section S3 in the Supporting Information. The thickness of the sputtered films was measured using a J.A. Woollam M-2000D spectroscopic ellipsometer at 75° incidence angle across 500 wavelengths from 190 to 1000 nm. Lamellae from select samples on c-sapphire substrates were prepared using a focused ion beam system with final thinning to ∼35 nm by Eurofins EAG Laboratories (Sunnyvale, CA). Transmission electron microscopy (TEM) and high-resolution TEM (HR-TEM) was performed using a Thermo-Fisher Talos F200X G2 instrument equipped with a 4k × 4k Ceta CMOS camera and double-tilt sample holder. All image processing and fast Fourier transform (FFT) analysis were performed using the Gatan Microscopy Suite.

Raman and Auger Spectroscopy. The highest and lowest thermal conductivity AlN films on both Si(111) and c-Al_2O_3 substrates were analyzed using Raman spectroscopy (Horiba Labram HR Evolution). Depth-profiling Auger spectroscopy was carried out using a 10 kV (10 nA) electron beam with samples deposited on Si(111) to avoid charging. Two measurements were collected before sputtering, and then additional measurements were collected after sputtering in 1 min increments to remove surface contamination and prevent carbon buildup, as described and plotted in Section S4 in the Supporting Information.

Time-Domain Thermoreflectance. The thermal conductivity of the AlN films was measured with time-domain thermoreflectance (TDTR), an optical pump−probe method used extensively to determine the thermal properties of nanoscopic materials.[30−32] Knife-edge measurements of the focused spot sizes provided $1/e^2$ beam radii of 5.36 ± 0.1 and 3.19 ± 0.05 for the pump and probe, respectively. Additionally, a pump modulation frequency of 10 MHz and total emitted power of 12.5 mW were applied. The reported mean values are determined from multiple measurements across the samples on different days, while the error bars represent one standard uncertainty determined from the standard deviations of the fitted values, uncertainties in the assumed parameters, and residuals between the model and data. Sensitivity analysis, calibration data, and additional thermal boundary conductance data are included in Section S6 and S9 in the Supporting Information.

ASSOCIATED CONTENT

Supporting Information

The Supporting Information is available free of charge at https://pubs.acs.org/doi/10.1021/acsnano.3c05485.

> Detailed descriptions and figures of the sputter deposition, X-ray diffraction analysis, Raman and Auger analysis, time-domain thermoreflectance (TDTR) measurements, TDTR sensitivity and uncertainty analyses, summary of all thermal boundary conductance values, the Boltzmann transport model used in this work, and secondary electrical breakdown tests (PDF)

AUTHOR INFORMATION

Corresponding Authors

Christopher Perez − *Department of Mechanical Engineering, Stanford University, Stanford, California 94305, United States; Materials Physics, Sandia National Laboratories, Livermore, California 94550, United States;* orcid.org/0000-0002-9628-2027; Email: cprez@alumni.stanford.edu

Suhas Kumar − *Materials Physics, Sandia National Laboratories, Livermore, California 94550, United States;* Email: su1@alumni.stanford.edu

Kenneth E. Goodson − *Department of Mechanical Engineering and Department of Materials Science and Engineering, Stanford University, Stanford, California 94305, United States;* Email: goodson@stanford.edu

Authors

Aaron J. McLeod − *Department of Chemistry and Biochemistry, University of California San Diego, La Jolla, California 92093, United States;* orcid.org/0000-0002-3720-0992

Michelle E. Chen − *Department of Materials Science and Engineering, Stanford University, Stanford, California 94305, United States*

Su-in Yi − *Department of Electrical and Computer Engineering, Texas A&M University, College Station, Texas 77843, United States*

Sam Vaziri − *Taiwan Semiconductor Manufacturing Company, San Jose, California 95134, United States*

Ryan Hood − *Materials Physics, Sandia National Laboratories, Livermore, California 94550, United States*

Scott T. Ueda − *Materials Science and Engineering Program, University of California San Diego, La Jolla, California 92093, United States*

Xinyu Bao − *Taiwan Semiconductor Manufacturing Company, San Jose, California 95134, United States*

Mehdi Asheghi − *Department of Mechanical Engineering, Stanford University, Stanford, California 94305, United States*

Woosung Park − *Division of Mechanical Systems Engineering, Sookmyung Women's University, Seoul 04310, South Korea*

A. Alec Talin − *Materials Physics, Sandia National Laboratories, Livermore, California 94550, United States;* orcid.org/0000-0002-1102-680X

Eric Pop − *Department of Electrical Engineering and Department of Materials Science and Engineering, Stanford University, Stanford, California 94305, United States;* orcid.org/0000-0003-0436-8534

Andrew C. Kummel − *Department of Chemistry and Biochemistry, University of California San Diego, La Jolla, California 92093, United States;* orcid.org/0000-0001-8301-9855

Complete contact information is available at:
https://pubs.acs.org/10.1021/acsnano.3c05485

Notes

The authors declare no competing financial interest.

ACKNOWLEDGMENTS

This work was supported in part by the Applications and Systems-Driven Center for Energy Efficient Integrated Nano Technologies (ASCENT), one of six centers in the Joint University Microelectronics Program (JUMP), an Semiconductor Research Corporation (SRC) program sponsored by the Defense Advanced Research Program Agency (DARPA). This work was performed in part at the San Diego Nanotechnology Infrastructure (SDNI) at UC San Diego, a member of the National Nanotechnology Coordinate Infrastructure, which is supported by the National Science Foundation (ECCS-1542148). Part of this work was performed at the Stanford Nano Shared Facilities (SNSF), supported by the National Science Foundation under award ECCS-1542152. We acknowledge the Laboratory Directed Research and Development program at Sandia National Laboratories, a multimission laboratory operated for the US Department of Energy (DOE)'s National Nuclear Security Administration under contract DE-NA0003525. This paper describes objective technical results and analyses. Any subjective views or opinions that might be expressed in the paper do not necessarily represent the views of the US Department of Energy or the United States Government. Part of this research conducted at both Sookmyung Women's University and Sogang University was supported by the National Research Foundation of Korea (NRF-2021R1C1C1008693).

REFERENCES

(1) Pop, E. Energy dissipation and transport in nanoscale devices. *Nano Research* **2010**, *3*, 147−169.

(2) Pop, E.; Varshney, V.; Roy, A. K. Thermal properties of graphene: Fundamentals and applications. *MRS Bulletin* **2012**, *37*, 1273−1281.

(3) Fu, Y.; et al. Graphene related materials for thermal management. *2D Materials* **2020**, *7*, 012001.

(4) Köroğlu, Ç.; Pop, E. High Thermal Conductivity Insulators for Thermal Management in 3D Integrated Circuits. *IEEE Electron Device Lett.* **2023**, *44* (3), 496−499.

(5) Oh, S. K.; Lundh, J. S.; Shervin, S.; Chatterjee, B.; Lee, D. K.; Choi, S.; Kwak, J. S.; Ryou, J.-H. Thermal Management and Characterization of High-Power Wide-Bandgap Semiconductor Electronic and Photonic Devices in Automotive Applications. *Journal of Electronic Packaging* **2019**, *141* (2), 020801.

(6) Xu, J.; Yin, W.-y.; Member, S.; Mao, J.; Member, S. Transient Thermal Analysis of GaN Heterojunction Transistors (HFETs) for High-Power Applications. *IEEE Microwave and Wireless Components Letters* **2007**, *17*, 55−57.

(7) Meneghesso, G.; Member, S.; Verzellesi, G.; Danesin, F.; Rampazzo, F.; Zanon, F.; Tazzoli, A.; Member, S.; Meneghini, M.; Member, S.; Zanoni, E.; Member, S.; et al. Reliability of GaN High-Electron-Mobility Transistors: State of the Art and Perspectives. *IEEE Transactions on Device and Materials Reliability* **2008**, *8*, 332−343.

(8) Wyrwas, E.; Condra, L.; Hava, A. Accurate Quantitative Physics-of-Failure Approach to Integrated Circuit Reliability. *IPC APEX EXPO Technical Conference*,2011; 3:1776, 1815.

(9) Wehmeyer, G.; Yabuki, T.; Monachon, C.; Wu, J.; Dames, C. Thermal diodes, regulators, and switches: Physical mechanisms and potential applications. *Applied Physics Reviews* **2017**, *4*, 041304.

(10) Sood, A.; Xiong, F.; Chen, S.; Wang, H.; Selli, D.; Zhang, J.; Mcclellan, C. J.; Sun, J.; Donadio, D.; Cui, Y.; Pop, E.; Goodson, K. E. An electrochemical thermal transistor. *Nature Communications* **2018**, *9*, 41866−41874.

(11) Chen, M. E.; Rojo, M. M.; Lian, F.; Koeln, J.; Sood, A.; Bohaichuk, S. M.; Neumann, C. M.; Garrow, S. G.; Goodson, K. E.; Alleyne, A. G.; Pop, E. Graphene-based electromechanical thermal switches. *2D Materials* **2021**, *8*, 035055.

(12) Li, J.; Nam, K.; Nakarmi, M.; Lin, J.; Jiang, H.; et al. Band structure and fundamental optical transitions in wurtzite AlN. *Appl. Phys. Lett.* **2003**, *83*, 5163−5165.

(13) Feneberg, M.; Leute, R. A. R.; Neuschl, B.; Thonke, K.; Bickermann, M. High-excitation and high-resolution photoluminescence spectra of bulk AlN. *Physical Review B* **2010**, *82*, 075208.

(14) Albrecht, J. D.; Chang, T.-h.; Kane, A. S.; Rosker, M. J.; Allen, B.; Drive, N. F., *DARPA's Nitride Electronic NeXt Generation Technology Program*. 2010, IEEE Compound Semiconductor Integrated Circuit Symposium (CSICS), Monterey, CA, USA, 2010.

(15) La Spina, L.; Iborra, E.; Schellevis, H.; Clement, M.; Olivares, J.; Nanver, L. Aluminum nitride for heatspreading in RF IC's. *Solid-State Electron.* **2008**, *52*, 1359−1363. Papers Selected from the 37th European Solid-State Device Research Conference - ESSDERC'07.

(16) Xu, R. L.; Rojo, M. M.; Islam, S.; Sood, A.; Vareskic, B.; Katre, A.; Mingo, N.; Goodson, K. E.; Xing, H. G.; Jena, D.; Pop, E. Thermal conductivity of crystalline AlN and the influence of atomic-scale defects Thermal conductivity of crystalline AlN and the in fl uence of atomic-scale defects. *J. Appl. Phys.* **2019**, *126*, 185105.

(17) He, Z.; Yan, Y.; Zhang, Z. Thermal management and temperature uniformity enhancement of electronic devices by micro heat sinks: A review. *Energy* **2021**, *216*, 119223.

(18) Cheng, Z.; et al. Experimental observation of high intrinsic thermal conductivity of AlN. *Physical Review Materials* **2020**, *4*, 044602.

(19) Kuo, P.; Auner, G.; Wu, Z. Microstructure and thermal conductivity of epitaxial AlN thin films. *Thin Solid Films* **1994**, *253*, 223−227.

(20) Koh, Y. R.; et al. Bulk-like Intrinsic Phonon Thermal Conductivity of Micrometer- Thick AlN Films. *ACS Applied Materials & Interfaces* **2020**, *12*, 29443−29450.

(21) Hoque, M. S. B.; et al. High In-Plane Thermal Conductivity of Aluminum Nitride Thin Films. *ACS Nano* **2021**, *15*, 9588−9599.

(22) Deprat, F.; Fenouillet-Beranger, C.; Jousseaume, V.; Guerin, C.; Beugin, V.; Rochat, N.; Licitra, C.; Caubet-Hilloutou, V.; Benoit, D.; Imbert, G.; Rambal, N.; Batude, P.; Vinet, M. Dielectrics stability for intermediate BEOL in 3D sequential integration. *Microelectron. Eng.*

2017, *167*, 90−94. Materials for Advanced Metallization 2016 (MAM 2016).

(23) Fenouillet-Beranger, C. et al. Guidelines for intermediate back end of line (BEOL) for 3D sequential integration. *2017 47th European Solid-State Device Research Conference (ESSDERC)*, 2017; pp 252−255.

(24) Schmitz, J. Low temperature thin films for next-generation microelectronics (invited). *Surf. Coat. Technol.* **2018**, *343*, 83−88. Selected papers of the "E-MRS 2017 − Symposium Q"

(25) Mion, C.; Muth, J. F.; Preble, E. A.; et al. Accurate dependence of gallium nitride thermal conductivity on dislocation density. *Appl. Phys. Lett.* **2006**, *89*, 092123.

(26) Beechem, T. E.; Mcdonald, A. E.; Fuller, E. J.; et al. Size dictated thermal conductivity of GaN Size dictated thermal conductivity of GaN. *J. Appl. Phys.* **2016**, *120*, 095104.

(27) Ueda, S. T.; McLeod, A.; Chen, M.; Perez, C.; Pop, E.; Alvarez, D.; Kummel, A. C. Deposition of High Thermal Conductivity AlN Heat Spreader Films. *2020 International Symposium on VLSI Technology, Systems and Applications, VLSI-TSA 2020* 2020; pp 110−111.

(28) McLeod, A. J.; Ueda, S. T.; Lee, P. C.; Spiegelman, J.; Kanjolia, R.; Moinpour, M.; Woodruff, J.; Kummel, A. C. Pulsed chemical vapor deposition for crystalline aluminum nitride thin films and buffer layers on silicon and silicon carbide. *Thin Solid Films* **2023**, *768*, 139717.

(29) Yalon, E.; Aslan, B.; Smithe, K. K. H.; McClellan, C. J.; Suryavanshi, S. V.; Xiong, F.; Sood, A.; Neumann, C. M.; Xu, X.; Goodson, K. E.; Heinz, T. F.; Pop, E. Temperature-Dependent Thermal Boundary Conductance of Monolayer MoS2 by Raman Thermometry. *ACS Applied Materials and Interfaces* **2017**, *9*, 43013−43020.

(30) Kwon, H.; Perez, C.; Park, W.; Asheghi, M.; Goodson, K. E. Thermal Characterization of Metal−Oxide Interfaces Using Time-Domain Thermoreflectance with Nanograting Transducers. *ACS Applied Materials Interfaces* **2021**, *13*, 58059−58065.

(31) Kwon, H.; Perez, C.; Kim, H. K.; Asheghi, M.; Park, W.; Goodson, K. E. Thermal Interface Enhancement via Inclusion of an Adhesive Layer Using Plasma-Enhanced Atomic Layer Deposition. *ACS Applied Materials and Interfaces* **2021**, *13*, 21905−21913.

(32) Perez, C.; Jog, A.; Kwon, H.; Gall, D.; Asheghi, M.; Kumar, S.; Park, W.; Goodson, K. E. Dominant Energy Carrier Transitions and Thermal Anisotropy in Epitaxial Iridium Thin Films. *Advanced Functional Materials* **2022**, *32*, 2207781.

(33) Jiang, P.; Qian, X.; Yang, R. Time-domain thermoreflectance (TDTR) measurements of anisotropic thermal conductivity using a variable spot size approach. *Rev. Sci. Instrum.* **2017**, *88*, 074901.

(34) Gaskins, J. T.; et al. Review—Investigation and Review of the Thermal, Mechanical, Electrical, Optical, and Structural Properties of Atomic Layer Deposited High- k Dielectrics: Beryllium Oxide, Aluminum Oxide, Hafnium Oxide, and Aluminum Nitride. *ECS Journal of Solid State Science and Technology* **2017**, *6*, N189−N208.

(35) Perez, C.; Knepper, R.; Marquez, M. P.; Forrest, E. C.; Tappan, A. S.; Asheghi, M.; Goodson, K. E.; Ziade, E. O. Non-Contact Mass Density and Thermal Conductivity Measurements of Organic Thin Films Using Frequency − Domain Thermoreflectance. *Advanced Materials Interfaces* **2021**, *9*, 2101404.

(36) Zhao, Y.; Zhu, C.; Wang, S.; Tian, J. Z.; Yang, D. J.; Chen, C. K.; Cheng, H.; Hing, P. Pulsed photothermal reflectance measurement of the thermal conductivity of sputtered aluminum nitride thin films. *J. Appl. Phys.* **2004**, *96*, 4563−4568.

(37) Choi, S. R.; Kim, D.; Choa, S.-h.; Lee, S.-h.; Kim, J.-k. Thermal Conductivity of AlN and SiC Thin Films. *International Journal of Thermophysics* **2006**, *27*, 896−905.

(38) Duquenne, C.; et al. Thermal conductivity of aluminium nitride thin films prepared by reactive magnetron sputtering. *Journal of Physics D: Applied Physics* **2012**, *45*, 015301.

(39) Pan, T. S.; Zhang, Y.; Huang, J.; Zeng, B.; Hong, D. H.; Wang, S. L.; Zeng, H. Z.; Gao, M.; Huang, W.; Lin, Y. Enhanced thermal conductivity of polycrystalline aluminum nitride thin films by optimizing the interface structure. *J. Appl. Phys.* **2012**, *112*, 044905.

(40) Aissa, K. A.; Semmar, N.; Achour, A.; Simon, Q.; Petit, A.; Camus, J.; Boulmer-Leborgne, C.; Djouadi, M. A. Achieving high thermal conductivity from AlN films deposited by high-power impulse magnetron sputtering. *Journal of Physics D: Applied Physics* **2014**, *47*, 355303.

(41) Bian, Y.; Liu, M.; Ke, G.; Chen, Y.; Dibattista, J.; Chan, E.; Yang, Y. Surface & Coatings Technology Aluminum nitride thin film growth and applications for heat dissipation. *Surface & Coatings Technology* **2015**, *267*, 65−69.

(42) Alvarez-Escalante, G.; Page, R.; Hu, R.; Xing, H. G.; Jena, D.; Tian, Z. High thermal conductivity and ultrahigh thermal boundary conductance of homoepitaxial AlN thin films. *APL Materials* **2022**, *10*, 011115.

(43) Slack, G. A.; Tanzilli, R.; Pohl, R.; Vandersande, J. The intrinsic thermal conductivity of AlN. *J. Phys. Chem. Solids* **1987**, *48*, 641−647.

(44) Rounds, R.; Sarkar, B.; Alden, D.; Guo, Q.; Klump, A.; Hartmann, C.; Nagashima, T.; Kirste, R.; Franke, A.; Bickermann, M.; Kumagai, Y.; Sitar, Z.; Collazo, R. The influence of point defects on the thermal conductivity of AlN crystals. *J. Appl. Phys.* **2018**, *123*, 185107.

(45) Jacquot, A.; Lenoir, B.; Dauscher, A.; Verardi, P.; Craciun, F.; Stolzer, M.; Gartner, M.; Dinescu, M. Optical and thermal characterization of AlN thin films deposited by pulsed laser deposition. *Appl. Surf. Sci.* **2002**, *186*, 507−512.

(46) Belkerk, B. E.; Camus, J.; Garnier, B.; Brithen, H. A.; Sahli, S.; Djouadi, M. A. Measuring anisotropic thermal conductivity of aluminum nitride films with the ultra-fast hot strip technique. *International Journal of Thermal Sciences* **2020**, *151*, 106259.

(47) Hirama, K.; Taniyasu, Y.; Kasu, M. AlGaN/GaN high-electron mobility transistors with low thermal resistance grown on single-crystal diamond (111) substrates by metalorganic vapor-phase epitaxy. *Appl. Phys. Lett.* **2011**, *98*, 162112.

(48) Chen, J.-T.; Pomeroy, J. W.; Rorsman, N.; Xia, C.; Virojanadara, C.; Forsberg, U.; Kuball, M.; Janzén, E. Low thermal resistance of a GaN-on-SiC transistor structure with improved structural properties at the interface. *J. Cryst. Growth* **2015**, *428*, 54−58.

(49) Shinoda, H.; Mutsukura, N. Structural properties of GaN and related alloys grown by radio-frequency magnetron sputter epitaxy. *Thin Solid Films* **2008**, *516*, 2837−2842.

(50) Kumada, T.; Ohtsuka, M.; Fukuyama, H. Influence of substrate temperature on the crystalline quality of AlN layers deposited by RF reactive magnetron sputtering. *AIP Advances* **2015**, *5*, 017136.

(51) Sproul, W.; Christie, D.; Carter, D. Control of reactive sputtering processes. *Thin Solid Films* **2005**, *491*, 1−17.

(52) Cho, J.; Francis, D.; Chao, P. C.; Asheghi, M.; Goodson, K. E. Cross-Plane Phonon Conduction in Polycrystalline Silicon Films. *Journal of Heat Transfer* **2015**, *137*, 071303.

(53) Matsunami, N.; Kakiuchida, H.; Sataka, M.; Okayasu, S. XRD Characterization of AlN Thin Films Prepared by Reactive RF-Sputter Deposition. *Advances in Materials Physics and Chemistry* **2013**, *03*, 101−107.

(54) El Akkad, F.; Marafi, M.; Punnoose, A.; Prabu, G. Effect of substrate temperature on the structural, electrical and optical properties of ITO films prepared by RF magnetron sputtering. *Physica Status Solidi (A) Applied Research* **2000**, *177*, 445−452.

(55) Gonçalves, C.; Charvet, S.; Zeinert, A.; Clin, M.; Zellama, K. Nanocrystalline silicon thin films prepared by radiofrequency magnetron sputtering. *Thin Solid Films* **2002**, *403-404*, 91−96.

(56) Jin, H.; Feng, B.; Dong, S.; Zhou, C.; Zhou, J.; Yang, Y.; Ren, T.; Luo, J.; Wang, D. Influence of substrate temperature on structural properties and deposition rate of AlN thin film deposited by reactive magnetron sputtering. *J. Electron. Mater.* **2012**, *41*, 1948−1954.

(57) Little, W. The transport of heat between dissimilar solids at low temperatures. *Canadian Journal of Physics* **1959**, *37*, 334−349.

(58) Swartz, E. T.; Pohl, R. O. Thermal boundary resistance. *Rev. Mod. Phys.* **1989**, *61*, 605−668.

(59) Monachon, C.; Weber, L.; Dames, C. Thermal Boundary Conductance: A Materials Science Perspective. *Annual Review of Materials Research* **2016**, *46*, 433−463.

(60) Liu, W.; Balandin, A. A. Thermal conduction in AlxGa1-xN alloys and thin films. *J. Appl. Phys.* **2005**, *97*, 073710.

(61) Yi, S. I.; Yu, C. Modeling of thermoelectric properties of SiGe alloy nanowires and estimation of the best design parameters for high figure-of-merits. *J. Appl. Phys.* **2015**, *117*, 035105.

(62) Yi, S. I.; Attari, V.; Jeong, M.; Jian, J.; Xue, S.; Wang, H.; Arroyave, R.; Yu, C. Strain-induced suppression of the miscibility gap in nanostructured Mg2Si-Mg2Sn solid solutions. *Journal of Materials Chemistry A* **2018**, *6*, 17559−17570.

(63) Morelli, D. T.; Heremans, J. P.; Slack, G. A. Estimation of the isotope effect on the lattice thermal conductivity of group IV and group III-V semiconductors. *Physical Review B - Condensed Matter and Materials Physics* **2002**, *66*, 1953041−1953049.

(64) Gaddy, B. E.; Bryan, Z.; Bryan, I.; Xie, J.; Dalmau, R.; Moody, B.; Kumagai, Y.; Nagashima, T.; Kubota, Y.; Kinoshita, T.; Koukitu, A.; Kirste, R.; Sitar, Z.; Collazo, R.; Irving, D. L. The role of the carbon-silicon complex in eliminating deep ultraviolet absorption in AlN. *Appl. Phys. Lett.* **2014**, *104*, 202106.

(65) Slack, G. A.; Glassbrenner, C. J. Thermal conductivity of Si and Ge from 3K to the melting point. *Phys. Rev.* **1964**, *134*, A1058−A1069.

(66) Morelli, D. T.; Beetz, C. P.; Perry, T. A. Thermal conductivity of synthetic diamond films. *J. Appl. Phys.* **1988**, *64*, 3063−3066.

(67) Lee, S. M.; Cahill, D. G. Heat transport in thin dielectric films. *J. Appl. Phys.* **1997**, *81*, 2590−2595.

(68) Jackson, A. W.; Ibbetson, J. P.; Gossard, A. C.; Mishra, U. K. Reduced thermal conductivity in low-temperature-grown GaAs. *Appl. Phys. Lett.* **1999**, *74*, 2325−2327.

(69) Ziade, E.; Yang, J.; Brummer, G.; Nothern, D.; Moustakas, T.; Schmidt, A. J. Thickness dependent thermal conductivity of gallium nitride. *Appl. Phys. Lett.* **2017**, *110* (3), 031903.

(70) Yan, R.; Simpson, J. R.; Bertolazzi, S.; Brivio, J.; Watson, M.; Wu, X.; Kis, A.; Luo, T.; Walker, A. R. H.; Xing, H. G. Thermal conductivity of monolayer molybdenum disulfide obtained from temperature-dependent Raman spectroscopy. *ACS Nano* **2014**, *8*, 986−993.

(71) Peimyoo, N.; Shang, J.; Yang, W.; Wang, Y.; Cong, C.; Yu, T. Thermal conductivity determination of suspended mono- and bilayer WS2 by Raman spectroscopy. *Nano Research* **2015**, *8*, 1210−1221.

(72) Lin, Z.; Liu, C.; Chai, Y. High thermally conductive and electrically insulating 2D boron nitride nanosheet for efficient heat dissipation of high-power transistors. *2D Materials* **2016**, *3*, 041009.

(73) Kang, J. S.; Li, M.; Wu, H.; Nguyen, H.; Hu, Y. Experimental observation of high thermal conductivity in boron arsenide. *Science* **2018**, *361*, 575−578.

(74) Chen, K.; et al. Ultrahigh thermal conductivity in isotope-enriched cubic boron nitride. *Science* **2020**, *367*, 555−559.

https://doi.org/10.1021/acsnano.3c05485
ACS Nano XXXX, XXX, XXX−XXX